Broad line quantitative chemical shift spectroscopy

W. T. Sobol, A. D. Elster, and W. H. Hinson
Department of Radiology, The Bowman Gray School of Medicine, Winston-Salem, North Carolina 27103

W. J. Chwals
Department of Surgery, The Bowman Gray School of Medicine, Winston-Salem, North Carolina 27103

Proton NMR spectroscopy was applied to quantitate the measurement of total body water/fat distributions *in vivo*. A special MR protocol was developed to excite a thick slab of tissue and display the magnitude NMR spectrum of the collected response signal. Very short echo time TE (8 ms) and long repetition time TR (4000 ms) were used to minimize relaxation damping of the signal intensities. The spectrum was then decomposed into individual lines and proton densities of different species were calculated. Proton density information was converted into weight percentage data using stoichiometrical and physiological information. The technique was validated using phantoms that contained different mixtures of water/maize oil. A high-resolution NMR spectrum of maize oil samples was used to determine the stoichiometric information. The test results showed good agreement with the known composition of the phantom within the whole range of water content (0–100%). This method is very fast since no phase encoding of data is required. Preliminary results for monkeys show promising potential in clinical applications.

Key words: nuclear magnetic resonance, NMR spectroscopy, water/fat distributions *in vivo*

I. INTRODUCTION

Several techniques have been proposed to suppress either the water or fat NMR signal in magnetic resonance (MR) imaging, using the difference in chemical shift of these two signals. The Dixon method and its variations explore phase differences between water and fat signals, created by an appropriate timing within the spin echo (SE) imaging protocol, to produce separate MR images of water and fat fractions from the same selected slice.[1,2] The selective excitation with chemical shift-specific slice selection uses a scheme that explores the chemical shift dependency of slice select positioning.[3,4] The selective saturation techniques use a soft pulse prior to the imaging sequence to saturate a desired spectral line or group of lines.[5–8] In addition, there are reports of MRI studies of fat using standard sequences (spin echo or inversion recovery) with imaging parameters selected to provide large image contrast between fat and other tissues.[9–11] All these approaches focus on the enhancement of water–fat signal contrast (by selectively suppressing signal from one of the species), in order to improve tissue discrimination for diagnostic purposes.

Recently, applications of MRI to body composition and nutrition studies have begun to emerge.[12] It is impractical, however, to obtain cross-sectional MR images that cover the entire body—it would take too much time to generate and process such data. Even if fast imaging sequences were used to generate MR images, relatively thin slices would have to be used to ensure proper classification of water and fat components (in thicker slices the volume averaging effects defeat the purpose). For an average person of 165-cm height, 165 slices of 1 cm would be required to cover the entire body. It takes about 30 min to classify lean tissue and fat areas within a single MR image with reasonable accuracy (custom image processing software and off-line computer hardware is need-

ed to achieve such throughput).[13,14] Therefore, the conventional approach is based upon standard anthropometric procedures, where only certain cross sections are evaluated (biceps, triceps, subscapular, and suprailiac locations). The total fat fraction within the body is then calculated using correlation formulas.[12] This approach has some obvious drawbacks (for example, the anthropometric correlation formulas do not account for fat deep inside the body). MR images can show all the fat within the imaged region, thus creating a question of statistical validity of correlations with techniques that do not account for deep fat depot. The most aggravating problem, however, relates to the fat quantification within the images. Since the technique requires the measurement of the percentage of the cross-sectional area occupied by adipose tissue, problems arise from motion artifacts and partial volume effects at tissue interfaces. This problem is most severe for lean bodies, since the margin of error, which remains approximately constant in absolute terms, produces large relative errors for cases with low adipose tissue content.

In this paper we present a technique that facilitates water/fat classification by applying an NMR spectroscopy technique in the imaging, slice selective manner.

II. METHOD

The experimental protocol for broad line quantitative chemical shift spectroscopy (MRI BCS) is shown in Fig. 1. First, magnetization is excited using a slice selective, imaging mode. Then, the echo is produced using a hard, nonselective π pulse. Data acquisition starts at the top of the echo and acquires half of an echo with no gradients present. There are several reasons for using such a protocol. First, the rf coil sensitivity distribution prevents collection of undistorted data from large volumes. Second, the NMR signal from a
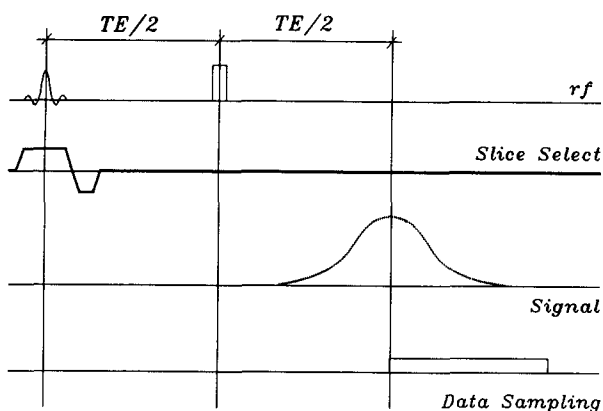
FIG. 1. The experimental protocol for broadline quantitative chemical shift spectroscopy.

large volume exceeds the dynamic range of the MR scanner's receiver channels. Thus slice selective excitation with a large (typically about 50 mm) slice thickness assures relatively undistorted NMR signals that fit into the signal ranges of existing hardware. Use of the slice selective excitation mode effectively prevents the collection of free induction decay (FID) signal since the initial part of FID is substantially distorted by the slice selection gradient. On the other hand, the echo protocol with an echo time TE produces a signal whose maximum is weighted with $\exp(- TE/T2)$. Since water and fat signals may have different spin–spin relaxation times ($T2$), this may produce systematic errors in signal intensity measurements. Therefore, the protocol uses hard π pulses to produce signals with very short TEs (the minimum value of TE is determined by the shape of slice select gradient, and typically is about 5–6 ms). The shape of the echo signal is determined by combined effects of rf distribution, magnetic field inhomogeneity, and eddy current effects and generally will not be a superposition of Lorentzian decays. Thus the variables $T2$ and $T2^*$ that are traditionally used to describe Lorentzian NMR signals related to spin–spin relaxation times and small magnetic field inhomogeneity effects have no meaning in the analysis of arbitrary echo shapes. The effective signal damping parameters (a for Lorentzian and σ for Gaussian shapes—see the Appendix) are used instead to describe signal shapes. Since no image is acquired, a very long repetition time TR can be used with no time penalty. The NMR signal is read without any gradient; thus the signal decay times (around $5 \times T2$) may last for several hundred ms. For very short echo times only a small fraction of the first half of the echo (during the TE/2 time between the rf and echo maximum) is formed (see Fig. 1). This effectively precludes the collection of the entire echo signal and leads to a scheme that utilizes only the second, undistorted part of the echo.

The NMR signal is collected in the phase sensitive quadrature mode, with the user having no control over the signal's phase. Thus after a Fourier transform (FT) is performed to produce an NMR spectrum, there is a variable, random phase error present in the spectrum. To correct this phase error, one would have to collect both real and imagi-

nary parts of the NMR signal and correct the phase in digital post-processing. This is impractical for very long signals since most MR scanners do not provide sufficient space to display both components with required accuracy (the user cannot get access to the raw digital data in a "single shot" mode). The practical solution to this problem is to produce a magnitude spectrum, register it on film, and manually digitize it for further processing. This magnitude spectral mode is standard on most MR scanners and is readily accessible. The NMR spectrum contains water and fat peaks shifted due to the chemical shift effects; if one separates these peaks, it is possible to retrieve information about FID amplitudes of each component. The FID amplitudes are proportional to the number of protons in each substance, thus such measurements provide a method for direct evaluation of proton densities of different materials within the excited slice. One can convert proton density information into weight percentages using stoichiometric information for each material.

The procedure can be repeated for several contiguous slices, simply by moving the subject inside the MR coil by a single slice thickness. The rf slice offset techniques should not be used to avoid variations introduced by volume distribution of rf coil sensitivity. This is a distinct advantage of this method, since it is relatively easy to produce data for the whole body, in contrast to traditional methods that use only partial measurements. The spectra are also easier to process than images, and much thicker slices used in MRI BCS reduce at least fivefold the number of data sets that must be acquired to cover the entire body.

III. VALIDATION

Despite the apparent simplicity of the proposed method, there are several factors that can affect the accuracy of results. The rf coil sensitivity distribution, and the imperfections in slice selection process are obvious examples. It is well known that rf coil sensitivity distribution affects the NMR signals in two ways: through changes of the effective tip angle during rf transmit mode and through differences in spatial sensitivity during signal acquisition.[15,16] Thus the rf coil must be tested first to check its quality. In general, specialty and surface coils should be avoided. A quadrature bird cage resonator head coil[17] was used in experiments described in this paper. A test using a uniform food phantom has shown that within the largest volume utilized in the experiments a signal nonuniformity was smaller than 5%, which was judged adequate. Such a good uniformity was assured by limiting the signal collection volume to the transverse slice in the center of the coil. A water/maize oil phantom model was used to test the accuracy of the protocol. The phantom consisted of ten plastic bottles of 30-ml capacity each. To avoid partial volume problems, the bottles were positioned entirely within the 50-mm-thick imaging plane. The bottles were filled with water or maize oil; thus it was possible to create a phantom that contained variable water/oil ratios by simply changing the number of bottles containing oil.

Tests were performed on a Picker Vista HP 2055 1.5T MR scanner. Eleven magnitude spectra were produced for phantoms containing 0–10 bottles of oil. All-water and all-oil

phantoms were used for control purposes. The experimental parameters were TE = 8 ms, TR = 4000 ms, 512 points acquisition matrix with 400 μs dwell time (sampling interval). The FT and magnitude spectra that spanned the range [− 1250,1250] Hz from the center (carrier) frequency were produced using standard features of the scanner. In cases where the water peak was present, the carrier was positioned at the center of the water peak. Spectra were recorded on film and then digitized using the Calcomp WIZ digitizing tablet, connected to a PC AT computer. The data were then transferred into the HP 9000/320 workstation for processing.

Custom software was written for the line decomposition process. A typical output from this program is shown in Fig. 2. The decomposition is performed interactively, using extensive graphics displays and mouse pointers. First, a line is fitted with a selected lineshape (by specifying center, amplitude, and half-width). Then, the fitted line is subtracted from the original data and the next line is fitted to residuals. When all lines are fitted, the composite lineshape is generated and the standard deviation calculated to assess the fit quality. The fitting process can be repeated interactively until a satisfactory fit is obtained. The fit quality is judged by the operator, who makes the decision whether to accept the current fit or to modify it. Adequate results (s.d. less than 5%) were routinely obtained for all the results discussed in this paper.

The selection of lineshape to fit the data is the pivotal point of the described routine. To assess the proton density associated with each line, one has to know the amplitude of its corresponding FID component. This parameter can be obtained by measuring either the amplitude and full width at half-maximum (FWHM), or the integral of the line. The relations between these parameters and FID amplitudes are derived in the Appendix. These derivations were performed for both echo and FID data of Lorentzian and Gaussian FID shapes (half-echo acquisition is equivalent to FID data, if one neglects $T2$ weighting). From preliminary experience it was found that most experimental data are better fitted with Gaussian FID profiles than with Lorentzian. We attribute

this finding to magnetic field inhomogeneity, slice profile imperfections, rf coil spatial sensitivity distribution, and residual eddy currents from a single, weak slice select gradient. All these detrimental effects determine the shape of the signal, thus mostly affecting the damping factors [parameter a in Eq. (A2), σ in Eq. (A12)]. Since the damping factors are excluded from TBW and TBF calculations, in principle, the magnetic field inhomogeneity should not lead to significant errors, as long as different spectral lines could be resolved with confidence.

The spectra for phantoms with different water/oil content were normalized first, to account for differences in signal intensity (MR scanner software provided access to both signal attenuation factor and FFT scaling factor). Then, the spectra were individually decomposed, and the individual lines were assigned to either oil or water. Figure 3 shows a spectrum of phantom that contained seven bottles of oil and three bottles of water. Such an interactive fit can be subject to an operator's subjective judgement. For example, a closer look at Fig. 2 (broad line spectrum of a phantom containing ten bottles of maize oil), Fig. 3 (broad line spectrum of a phantom containing seven bottles of oil and three bottles of water), and Fig. 4 (HR NMR spectrum of maize oil solution in $CDCl_3$) reveals that the broad line spectra do not always closely resemble the HR NMR spectrum of oil solution. After some tests it was concluded that the magnetic field inhomogeneity, rf coil spatial resolution, and residual eddy current effects from the single, small slice select gradient, affect the shape of the spectrum. For different phantom configurations various minor spectral lines will either entirely blend with major peaks (H_2O or CH_2), or show up as "bulges" on the shoulders of major peaks. As a result, attempts to resolve those "shoulders" will lead to minor lines at different frequencies. Since it is known that water generates only a single NMR line, these minor peaks were counted as oil contributions. This way, the proton densities from minor peaks were either counted separately, or contributed to the CH_2 peak. Unfortunately, two minor oil components: one around 5.4 ppm (from -CH = CH- protons) and the other at 4.2 ppm (from -CH-CH$_2$-O-CO-R protons) can sometimes blend into the water peak (at 4.9 ppm) and con-
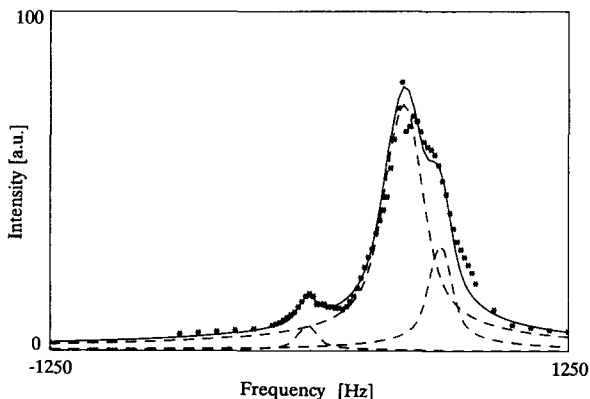

FIG. 2. A typical output of the peak decomposition program. Stars show digitized points of the original magnitude spectrum (pure maize oil). Broken lines show individual components, and the solid line shows the final composite spectrum.
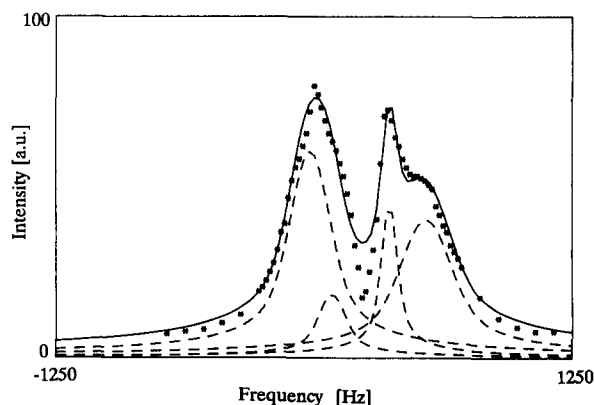

FIG. 3. The magnitude spectrum for a phantom with seven oil and three water bottles. The leftmost line represents water, the remaining three were classified as oil.
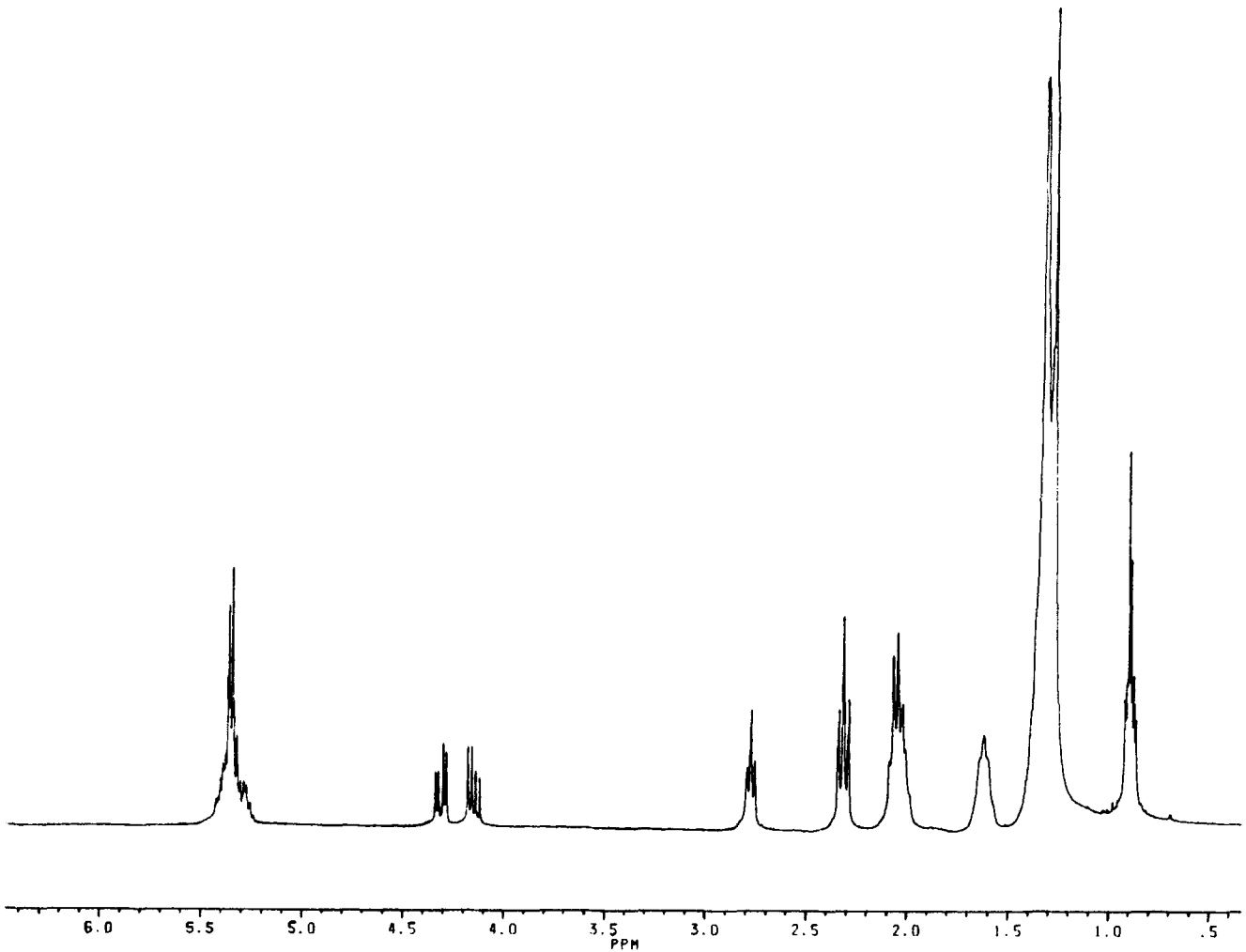
Fig. 4. The high resolution NMR spectrum of oil used in the phantom.

tribute to an error in the accuracy of results.

For each line, the corresponding FID amplitude was calculated using both amplitude/width and integral methods. For the Gaussian lineshape that corresponds to the half-echo collection scheme, the FID amplitude A can be calculated either from spectrum amplitude $M(0)$ and its FWHM W using Eq. (A24)

$$A = 0.19337[M(0)/W] \tag{1}$$

or from the spectrum integral S [Eq. (A24)]:

$$A = 0.10992S. \tag{2}$$

The differences between these two methods did not exceed 5%. Once the lines were assigned and processed, the relative spin densities for water and oil were known. The term "relative" refers to the fact that FID amplitudes are proportional to spin densities, but the proportionality constant is always an unknown factor that depends on scanner's hardware. In cases where absolute values are needed, the data can be calibrated using an additional bottle that contains material with the NMR signal away from both water and oil signals. Chloroform, with a single peak at around 7 ppm, may be used, but its low proton density requires the use of relatively

large volumes to ensure that the reference peak will appear in the spectrum. Preliminary studies have shown that such a standard did not lead to any significant improvement in the quality of results, while it added complications to the line resolving process. Thus relative signal intensities were utilized in the method.

To convert the relative spin density data into weight percentage data, stoichiometric information about substances is needed. The composition of water is trivial, but fat is another matter. It was assumed that the "fat" NMR signal arises only from triglycerides. The average fatty acid composition of different "fat" materials is known.[18] The data for maize oil and human fat are shown in Fig. 5. This average distribution was checked for maize oil used in the phantom. The HR NMR spectrum of oil was recorded on a Bruker AM 300-MHz NMR spectrometer (Fig. 4). The individual lines were then assigned using literature data.[19] The spin densities, evaluated from average distribution data (Fig. 5) were within 10% of the integral values for individual lines. This justified the use of data in Fig. 5 for phantom's maize oil. The published spectra similarly justify the use of average data in Fig. 5 for human fat.[20]
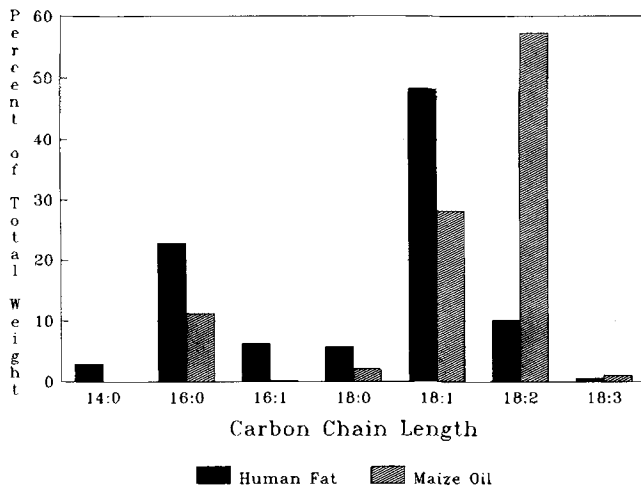
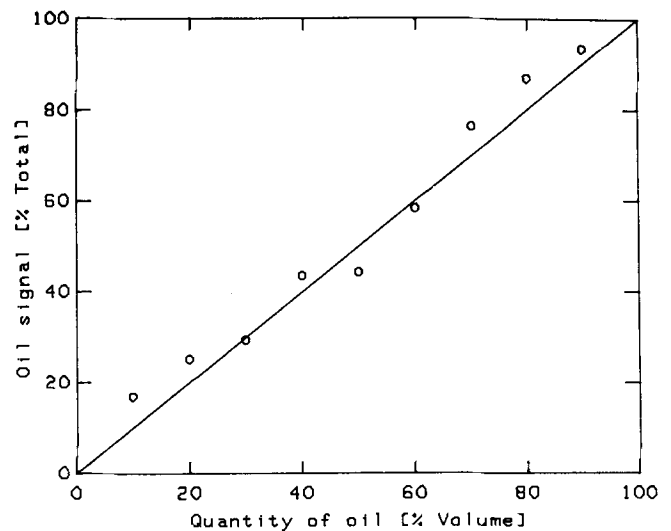FIG. 5. The fatty acid distribution for maize oil and human fat.

FIG. 6. The weight percent of oil, calculated from NMR spectra, vs. the relative volume of oil in the phantom. Solid line shows the identity relation.

From the fatty acid distribution data, the average molecular weight and average proton content per mole of triglycerides was calculated. For maize oil, the molecular weight was 871.98 g, with 99.7511 N protons per mole (N is the Avogadro number). For human fat, the molecular weight is 854.28 g and number of protons per mole is 100.7297 N. With these results, it is possible to calculate proton density/weight conversion factors. For simplicity of conversion, the factor for water can be made unity, and water proton density factor incorporated into fat conversion factor. For maize oil, this factor is 0.970745, for human fat 0.941798. Thus if A_w and A_0 represent FID amplitudes for water and oil, respectively, then the weight fraction of oil is equal to

$$ m[\%] = \frac{0.970745A_0}{A_w + 0.970745A_0} \times 100\%. \tag{3} $$

The numerical constants in this equation are deliberately specified well beyond the expected accuracy of experimental values A_w and A_0, to avoid round off errors for any experimental data (in normal conditions experimental data are known with a three digit precision). The weight fraction data, calculated from NMR magnitude spectra for nine different phantom compositions, are shown in Fig. 6. These results show that the method is capable of producing accurate results.

IV. DISCUSSION

The method described was developed in response to the need to evaluate the body cell mass (BCM) in preoperative neonates and infants in order to assess the ability of the body to handle the post-operative stress. To find BCM, the values of body weight (BW), total body water (TBW), and total body fat (TBF) are needed, as well as fat free solids (FFS) and intracellular body water (ICW).[20] These variables are global, i.e., they include contributions from all the tissues in the body. For example, TBF includes all the fat and fatty components (like bone marrow) from the body, regardless of distribution. The goal of a clinical study presently under way is to determine whether the BCM can be determined

with acceptable accuracy from the measurements to BW, TBW, and TBF. This study uses as an animal model adult *Macaca fascicularis* monkeys and tests several known methods of body composition measurements (isotope dilution technique as a "gold standard", measurements of body resistivity, ultrasound, CT, and MR imaging methods). Since the MRI BCS method seemed to provide a quick, safe, and noninvasive way to evaluate the TBF and TBW, the next step after phantom validation involved *in vivo* tests of the protocol using this animal model.

Sedated adult monkeys were placed individually on an animal holder with a calibrated scale on its side. This holder was then placed into the MR head coil in such a manner that MR spectra could be recorded from consecutive, contiguous 50-mm slices. On average, the 10–12 slices needed to cover an entire animal required about 20 min, including the acquisition of a pilot image (typical results are shown in Fig. 7). For comparison, Fig. 8 shows an MR image of the monkey
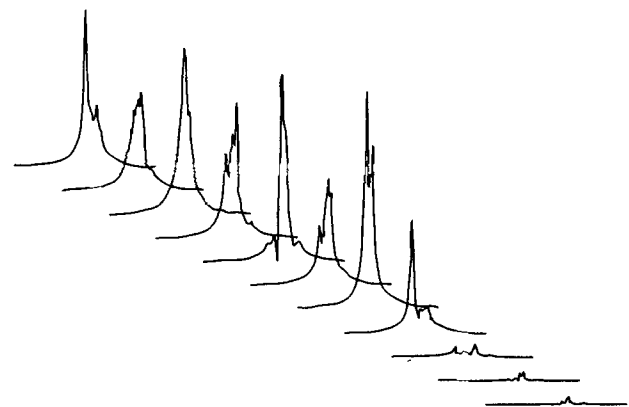

FIG. 7. A typical set of spectra for an entire monkey. The top left spectrum covers the head, the bottom right—the tail. All spectra shown in the same scale.
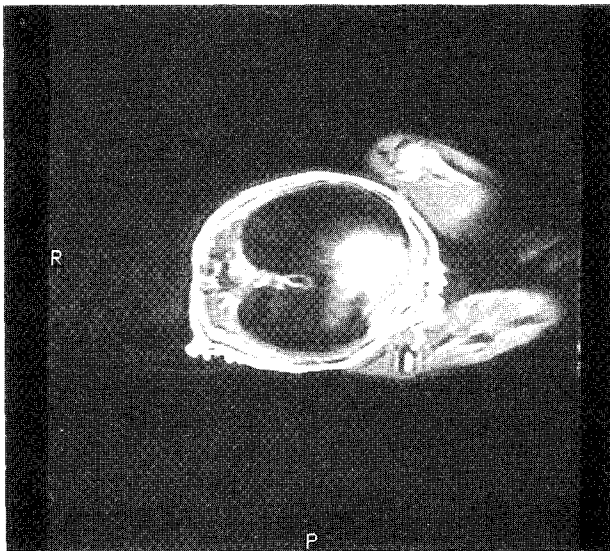
FIG. 8. A typical MR image of the abdominal region of the monkey. Note partial volume effects that make fat classification task difficult.
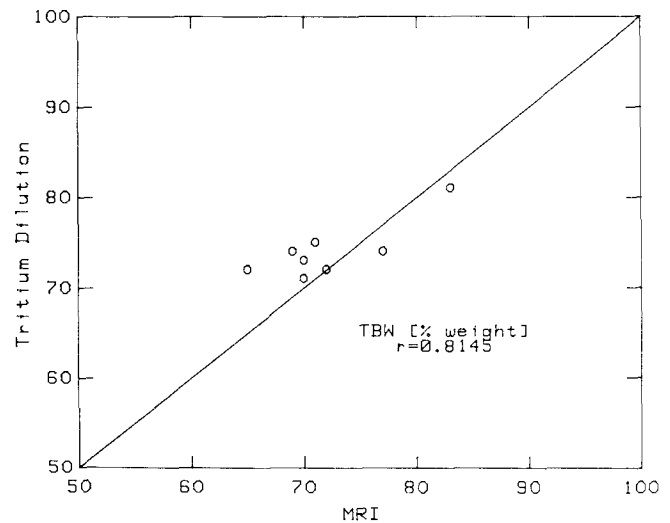

FIG. 9. A comparison of TBW values determined using the tritium dilution and MRI BCS methods. Data shown for eight different animals, the identity line is shown for reference.

abdominal area, which normally would be used for water/fat assessment. Such images were used to assess the TBW and TBF using water/fat classification methods. Efforts that utilized special image processing techniques (histogram analysis and region growing), were consistently inferior to results obtained from MRI BCS method, due to large errors caused by motion artifacts and partial volume effects at fat/tissue interfaces. In the monkeys, these errors could reach 50%–60%, due to the leanness of the animals. On the other hand, the MRI BCS technique does not provide information about spatial distribution of fat, and obviously cannot be used in studies that require such information.

Our preliminary studies indicate that the protocol works *in vivo* as well. In Fig. 9 the data for eight animals are used to compare the TBW values determined using the tritium dilution and the MRI BCS methods. The largest difference between both methods was 6.9%, the average difference was 3.3%, the correlation coefficient was $r = 0.8145$. The advantage of MRI BCS over traditional techniques lies in the access to the data for the whole body, not just for a particular area. However, the information about tissue distribution is lacking. There is no time penalty in the data acquisition (it takes comparable time to produce set of spectra and an image). The analysis of spectra is easier than attempts to classify fat within an image, especially for a lean body. So far, the only limitation discovered is related to the motion artifacts in the abdominal area. Due to the respiratory motion, the spectrum is unstable to some degree (repetitive acquisitions show different results with up to 20% variation in the amplitude of the major peak). One way to circumvent this problem is to wait several TR cycles and register the spectrum that is most stable.

Factors that affect the accuracy of the proposed method (magnetic field inhomogeneity, rf coil sensitivity distribution, eddy current effects, errors in line decomposition) must be weighed against limitations of other available tech-

niques. Tritium dilution, for example, requires monitoring body fluids balance for at least 24 hr. The logistics of collecting all the urine, produced by a healthy animal who does not like wearing diapers, poses a challenging problem that often leads to significant errors in accuracy of the results. All other techniques (caliper measurements, single slice imaging methods, body resistivity methods) use correlation tables and nomograms to derive TBW; thus they provide statistical indicators rather than precise results. In this light, a method that is clearly crude when compared to HR NMR spectroscopy *in vitro*, appears to be a reasonable choice among other currently available methods to measure TBW and TBF.

In conclusion, the proposed method shows promising results. It is simple, fast, noninvasive, and easy to implement. After final validation, it is intended for use in the clinical studies of metabolic stress in an animal model, with extension to human infants. It can easily be applied to the studies of humans, as long as the large field of view, required to accommodate some people, will not cause the larger magnetic field inhomogeneities to broaden the individual NMR lines beyond possible resolution. Our experience with MR imaging protocols that suppress either water or fat signal using its chemical shift properties[13,14] shows that MRI BCS method could be useful in human studies that require global assessment of TBW and TBF, without the need for information about tissue distribution within the body.

APPENDIX

It may seem that the task of calculating magnitude spectra of simple NMR signals is trivial. This is only partially true. For the reader's convenience, in this appendix we provide results for FID and echo signals of Lorentzian and Gaussian shapes. The Fourier transform (FT) formulas come in several variations, but the following forms are used in this Appendix:

$$F(\omega) = \int_{-\infty}^{\infty} f(t)e^{-i\omega t}\,dt,$$

$$f(t) = \frac{1}{2\pi}\int_{-\infty}^{\infty} F(\omega)e^{i\omega t}\,d\omega. \tag{A1}$$

1. Lorentzian shapes

A. Free induction decay (FID) signal

The Lorentzian signal (either FID or half-echo acquisition) has the form

$$f(t) = Ae^{i\varphi}e^{-at+i\omega_0 t}u(t), \tag{A2}$$

where A is the amplitude, φ is the phase, ω_0 is the frequency offset, a is the damping parameter ($a = 1/T2$ in the ideal case of liquids, $1/T2^*$ for small magnetic field inhomogeneities across liquid samples, and has no simple meaning otherwise) and

$$u(t) = \begin{cases} 1, & t \geqslant 0, \\ 0, & t < 0. \end{cases} \tag{A3}$$

The FT is easily obtained, direct integration yields

$$F(\omega) = \frac{Ae^{i\varphi}}{a+i(\omega-\omega_0)} = Ae^{i\varphi}\frac{a-i(\omega-\omega_0)}{a^2+(\omega-\omega_0)^2}; \tag{A4}$$

and, consequently, the magnitude spectrum is

$$M(\omega) = \sqrt{[\operatorname{Re}F(\omega)]^2 + [\operatorname{Im}F(\omega)]^2}$$

$$= A/\sqrt{a^2+(\omega-\omega_0)^2}. \tag{A5}$$

The goal is to determine the amplitude A from the FT magnitude spectrum. This can be achieved either by measuring the full width at half-maximum (FWHM) W and the FT spectrum amplitude $M(0)$, or by measuring the area under the line (integral S). By direct integration one discovers that the integral diverges (the well-known problem of "Lorentzian wings"). Therefore, a practical solution is to integrate over an interval spanning five FWHM on each side of the line. Thus

$$M(0) = A/a,$$

$$W = 2\sqrt{3}a$$

$$S = \int_{-\infty}^{\infty} P(\omega)d\omega \approx \int_{-10a\sqrt{3}}^{+10a\sqrt{3}} \frac{A}{\sqrt{a^2+x^2}}\,dx$$

$$= [A\ln(x+\sqrt{x^2+a^2})]_{-10a\sqrt{3}}^{+10a\sqrt{3}}$$

$$\approx 7.092\,A. \tag{A6}$$

B. Echo signal

The Lorentzian signal (when entire NMR echo signal is acquired—its envelope is formed by two back-to-back exponentials with the echo maximum at $t = 0$ since there is a modulus of time in the damping term) has a form

$$f(t) = Ae^{i\varphi}e^{-a|t|+i\omega_0 t}, \tag{A7}$$

and its FT is easy to evaluate:

$$F(\omega) = 2aAe^{i\varphi}/[a^2+(\omega-\omega_0)^2]. \tag{A8}$$

Its magnitude spectrum is

$$M(\omega) = 2aA/[a^2+(\omega-\omega_0)^2]. \tag{A9}$$

In this case, the value of integral S can be independently checked using a feature

$$f(0) = \frac{1}{2\pi}\int_{-\infty}^{+\infty} F(\omega)d\omega, \tag{A10}$$

which follows from Eq. (A1). Therefore,

$$M(0) = 2A/a,$$

$$W = 2a$$

$$S = \int_{-\infty}^{+\infty} P(\omega)d(\omega) = 2A\int_{-\infty}^{+\infty} \frac{1}{1+y^2}\,dy = 2\pi A. \tag{A11}$$

2. Gaussian shapes

We will start with the echo signal, which is easier to evaluate.

A. Echo signal

Gaussian echo signal (its envelope is a full Gaussian bell curve) is defined as

$$f(t) = Ae^{i\varphi}e^{-t^2/2\sigma^2+i\omega_0 t} \tag{A12}$$

and its FT is

$$F(\omega) = Ae^{i\varphi}\int_{-\infty}^{+\infty} e^{-i(\omega-\omega_0)t}e^{-t^2/2\sigma^2}\,dt$$

$$= Ae^{i\varphi}e^{-\sigma^2(\omega-\omega_0)^2/2}$$

$$\times \int_{-\infty}^{+\infty} e^{-[t+i\sigma^2(\omega-\omega_0)]^2/2\sigma^2}\,dt$$

$$= A\sigma e^{i\varphi}\sqrt{2}e^{-\sigma^2(\omega-\omega_0)^2/2}\int_{-\infty}^{+\infty} e^{-x^2}\,dx$$

$$= \sqrt{2\pi}A\sigma e^{i\varphi}e^{-\sigma^2(\omega-\omega_0)^2/2}. \tag{A13}$$

This derivation utilizes the Cauchy's theorem for integrals of complex variables. Since the function has no poles, its integral over any closed path vanishes. Thus consider a rectangular path whose one side is formed by the real axis t and the other, parallel side is offset by some imaginary value iz. The path is closed by two shunts at $t = \pm\infty$. Since the function vanishes at infinity, the shunts do not contribute to the integral. Therefore, an integration path along any complex straight line parallel to the real axis yields identical result as the integration along the real axis; the integration path can thus be modified from complex to real. The magnitude spectrum is

$$M(\omega) = \sqrt{2\pi}A\sigma e^{-\sigma^2(\omega-\omega_0)^2/2}. \tag{A14}$$

Therefore,

$$M(0) = \sqrt{2\pi}A\sigma,$$

$$W = 2\sqrt{2\ln 2}/\sigma,$$

$$S = \int_{-\infty}^{+\infty} P(\omega)d(\omega) = \sqrt{2\pi}A\sigma \int_{-\infty}^{+\infty} e^{-\sigma^2(\omega - \omega_0)^2/2} d\omega$$

$$= 2\sqrt{\pi}A \int_{-\infty}^{+\infty} e^{-x^2} dx$$

$$= 2\pi A. \tag{A15}$$

B. FID shape

The Gaussian signal (FID or half-echo) has the form

$$f(t) = Ae^{i\varphi}e^{-t^2/2\sigma^2 + i\omega_0 t}u(t). \tag{A16}$$

Calculations similar to those performed for the Gaussian echo signal quickly yield

$$F(\omega) = Ae^{i\varphi}e^{-\sigma^2(\omega - \omega_0)^2/2} \int_0^{+\infty} e^{-[t + i\sigma^2(\omega - \omega_0)]^2/2\sigma^2} dt. \tag{A17}$$

Introducing two new variables

$$\Omega = \sigma(\omega - \omega_0)/\sqrt{2},$$

$$x = t/\sigma\sqrt{2} + \Omega; \tag{A18}$$

we obtain

$$F(\Omega) = \sqrt{2}A\sigma e^{i\varphi}e^{-\Omega^2} \int_{i\Omega}^{+\infty} e^{-x^2} dx$$

$$= \sqrt{2}A\sigma e^{i\varphi}e^{-\Omega^2} \left(\int_0^{+\infty} e^{-x^2} dx - \int_0^{i\Omega} e^{-x^2} dx \right)$$

$$= \sqrt{(\pi/2)}A\sigma e^{i\varphi}e^{-\Omega^2}[1 - \mathrm{erf}(i\Omega)]. \tag{A19}$$

This result can be independently obtained using Ryzhik's formula (3.222).[22] It is easy to show, using variable substitution, that

$$\int_0^{ix} e^{-t^2} dt = i \int_0^x e^{t^2} dt. \tag{A20}$$

Therefore, the FT spectrum of the Gaussian FID can be written as

$$F(\Omega) = \sqrt{\frac{\pi}{2}} A\sigma e^{i\varphi}e^{-\Omega^2}\left(1 - \frac{2i}{\sqrt{\pi}} \int_0^{\Omega} e^{t^2} dt \right)$$

$$= A\sigma e^{i\varphi}\left[\sqrt{\frac{\pi}{2}} e^{-\Omega^2} - \sqrt{2}i \, \mathrm{daw}(\Omega)\right], \tag{A21}$$

where daw(x) is the Dawson function, defined as

$$\mathrm{daw}(x) = \int_0^x e^{t^2 - x^2} dt. \tag{A22}$$

The Dawson function is very similar in shape to the dispersive (imaginary component) of the Lorentzian FT spectrum, but its values must be evaluated numerically. Spanier[23] provides a very effective algorithm that guarantees 24-bit precision (relative error is always smaller than $6*10^{-8}$). The following code shows the implementation of this algorithm in HP BASIC (it can easily be modified for other languages):

```
DEF FNDawson(REAL X)
REAL X1,X2,F,P
INTEGER J
   X1=ABS(X)
   X2=X*X
   SELECT X1
      CASE =0
         RETURN 0
      CASE <5
         J=1+INT(12*SQR(X1))
         P=J+0.5-INT(X2)
         F=X2/P
         REPEAT
            P=P-1
            F=X2*(F/J+1/P)
            J=J-1
         UNTIL J=0
         F=F*EXP(-X2)
      CASE >=5
         P=-1.5-INT(30/X1)
         F=1
      END SELECT
      WHILE P<0
         F=1-P*F/X2
         P=P+1
      END WHILE
      RETURN F/(2*X)
FNEND
```

The magnitude FT spectrum is

$$M(\Omega) = A\sigma\sqrt{(\pi/2)e^{-2\Omega^2} + 2\,\mathrm{daw}^2(\Omega)}. \tag{A23}$$

Both FWHM and S have to be determined numerically. For the experimental magnitude spectrum $M(\omega)$ one obtains, using the five FWHM criterion for the limits of S:

$$M(0) = \sqrt{(\pi/2)}A\sigma,$$

$$W = 4.126142654/\sigma,$$

$$S = 9.0978430A. \tag{A24}$$

[1] W. T. Dixon, "Simple Proton Spectroscopic Imaging," Radiology **153**, 189–194 (1984).

[2] J. K. T. Lee, W. T. Dixon, D. Ling, R. G. Levitt, and W. A. Murphy, "Fatty Infiltrations of the Liver: Demonstration by Proton Spectroscopic Imaging," Radiology **153**, 195–201 (1984).

[3] H. W. Park, D. J. Kim, and Z. H. Cho, "Gradient-Reversal Technique and Its Applications to Chemical-Shift-Related NMR Imaging," Magn. Reson. Med. **4**, 526–536 (1987).

[4] A. Volk, B. Tiffon, J. Mispelter, and J. M. Lhoste, "Chemical Shift-Specific Slice Selection. A New Method for Chemical Shift Imaging at High Magnetic Field," J. Magn. Reson. **71**, 168–174 (1987).

[5] B. R. Rosen, V. J. Wedeen, and T. J. Brady, "Selective Saturation NMR Imaging," J. Comp. Assist. Tomogr. **8**, 813–818 (1984).

[6] L. Axel and L. Dougherty, "Chemical Shift Selective MRI of multiple-line Spectra by Selective Saturation," J. Magn. Reson. **66**, 194–196 (1986).

[7] A. Haase, J. Frahm, W. Hanicke, and D. Matthaei, "1H NMR Chemical Shift Selective (CHESS) Imaging," Phys. Med. Biol. **30**, 341–344 (1985).

[8] P. M. Joseph and A. Shetty, "A Comparison of Selective Saturation and Selective Echo Chemical Shift Imaging Techniques," Magn. Reson. Imag. **6**, 421–430 (1988).

[9] M. A. Foster, J. M. S. Hutchison, J. R. Mallard, and M. Fuller, "NMR Pulse Sequence and Discrimination of High- and Low-Fat Tissues," Magn. Reson. Imag. **2**, 187–192 (1984).

[10] G. C. Dooms, H. Hricak, A. R. Margulis, and G. de Geer, "MR Imaging of Fat," Radiology **158**, 51–54 (1986).

[11] J. C. Seidell, C. J. G. Bakker, and K. van der Kooy, "Imaging Techniques for Measuring Adipose Tissue Distribution—A Comparison between CT and 1.5T MR," Am. J. Clin. Nutr. **51**, 953–957 (1990).

[12] L. E. Preuss and F. P. Bolin, "Biophysical Methods for Estimating In Vivo Body Composition: The Determination of Adipose Compartment," Henry Ford Hosp. Med. J. **36**, 92–102 (1988).

[13] S. Roessner, W. J. Bo, E. Hiltbrandt, W. Hinson, N. Karstaedt, P. Santago, W. T. Sobol, and J. R. Crouse, "Adipose Tissue Determinations in Cadavers—A Comparison Between Cross-sectional Planimetry and Computed Tomography," Int. J. Obesity **14**, 893–902 (1990).

[14] W. T. Sobol, S. Roessner, W. Hinson, E. Hiltbrandt, N. Karstaedt, P. Santago, N. Wolfman, A. Hagaman, and J. R. Crouse, "Evaluation of a New MRI Method for Quantitating Adipose Tissue Areas," Int. J. Obesity **15**, 589–599 (1991).

[15] R. K. Breger, F. W. Wehrli, H. C. Charles, J. R. MacFall, and V. M. Haughton, "Reproducibility of Relaxation and Spin-Density Parameters in Phantoms and the Human Brain Measured by MR Imaging at 1.5T," Magn. Reson. Med. **3**, 649–662 (1986).

[16] W. H. Hinson and W. T. Sobol, "A New Method of Computing Spin-Lattice Relaxation Maps in MRI Using Fast Scanning Protocols," Med. Phys. **15**, 551–561 (1988).

[17] J. Tropp, "The Theory of a Birdcage Resonator," J. Magn. Reson. **82**, 51–62 (1989).

[18] *The Lipid Handbook*, edited by F. D. Gunstone, J. L. Harwood, and F. B. Padley (Chapman and Hall, New York, 1986).

[19] D. J. Frost and F. D. Gunstone, "The PMR Analysis of Non-conjugated Alkenoic and Alkynoic Acids and Esters," Chem. Phys. Lipids **15**, 53–85 (1975).

[20] R. L. Kamman, K. G. Go, F. A. J. Muskiet, G. P. Stomp, P Van Dijk, and H. J. C. Berendsen, "Proton Spin Relaxation Studies of Fatty Tissue and Cerebral White Matter," Magn. Reson. Imag. **2**, 211–220 (1984).

[21] F. D. Moore, K. H. Olesen, J. D. McMurrey, A. V. Parker, M. R. Ball, and C. M. Boyden, *The Body Cell Mass and its Supporting Environment* (Saunders, Philadelphia, 1963).

[22] I. S. Gradshteyn and I. M. Ryzhik, *Table of Integrals, Series, and Products* (Academic, San Diego, 1980).

[23] J. Spanier and K. B. Oldham, *An Atlas of Functions* (Hemisphere, New York, 1987), p. 389.